Laser photothermal radiometric instrumentation for fast in-line industrial steel hardness inspection and case depth measurements

Xinxin Guo,[1,2,*] Konesh Sivagurunathan,[1] Jose Garcia,[1,2] Andreas Mandelis,[1,2] Salvatore Giunta,[3] and Salvatore Milletari[3]

[1]Center for Advanced Diffusion-Wave Technologies (CADIFT), Department of Mechanical and Industrial Engineering, University of Toronto, 5 King's College Road, Toronto M5S 3G8, Canada

[2]Photo-Thermal Diagnostics, 243 College Street, Toronto M5T 1R5, Canada

[3]Department of Industrial Technologies, Avio S.p.A., Via I Maggio 99, 10040 Rivalta di Torino, Italy

*Corresponding author: guox@mie.utoronto.ca

Received 19 August 2008; accepted 15 September 2008;
posted 24 September 2008 (Doc. ID 100084); published 22 October 2008

A contact-free, nondestructive laser photothermal radiometric instrumentation technique was developed to meet industrial demand for on-line steel hardness inspection and quality control. A series of industrial steel samples, flat or curvilinear, with different effective hardness case depths ranging between 0.21 and 1.78 mm were measured. The results demonstrated that three measurement parameters (metrics) extracted from fast swept-sine photothermal excitation and measurements, namely, the phase minimum frequency $f_{\min}$, the peak or trough frequency width W, and the area S, are complementary for evaluating widely different ranges of hardness case depth: $f_{\min}$ is most suitable for large case depths, and W and S for small case depths. It was also found that laser beam angular inclination with respect to the surface plane of the sample strongly affects hardness measurement resolution and that the phase frequency maximum is more reliable than the amplitude maximum for laser beam focusing on the sample surface. © 2008 Optical Society of America

OCIS codes: 120.0280, 120.4290, 160.3900, 350.5340.

1. Introduction

Photothermal (PT) techniques are widely used detection schemes for an optical-source-induced temperature rise in condensed matter and/or in adjacent fluid/gaseous media. They include photoacoustic spectroscopy [1], photothermal radiometry (PTR) [2], photopyroelectric thermal-wave cavity detection [3], and photothermal beam deflection [4]. These techniques have played an important role in nondestructive testing for thermophysical property measurements as well as for surface/subsurface defect detection [5–7]. They are capable of nondestructive characterization of subsurface features of the order of a few micrometers to millimeters in depth in composite or inhomogeneous materials through thermal-diffusion-length probing by scanning the modulation frequency of the incident laser power. This feature of the photothermal techniques has been used effectively in the evaluation of discretely layered structures [8–10]. In recent years, PT technologies have extended their applications to inhomogeneous materials with continuously varied properties. One example is the nondestructive evaluation of the case depth profile of hardened steels. The surface structure of a case-hardened sample is an inhomogeneous layer with continuously varying thermophysical parameters from the surface to the unhardened subsurface of the sample. Anticorrelation between thermal diffusivity or thermal conductivity and

0003-6935/09/070C11-13$15.00/0

microhardness has been reported by several research groups [11–14].

The performance of surface hardened steel parts is a major issue in automotive and aerospace industries. There is a strong need for hardening and heat treating companies to improve the quality control of their products by introducing new inspection systems that allow for nondestructive, noncontacting hardness profile measurements as an alternative to the destructive indenter-based inspection methods used at present. The PTR phase frequency minimum is the result of thermal-wave interference [15] within the hardened layer, thus becoming a measure of effective hardness case depth. This determines the effectiveness of PTR technology in hardness inspection. It has been the aim of this work to develop a contact-free, calibrated nondestructive photothermal instrumentation and measurement principle, an important step toward achieving full on-line production control. We present the physical principles, instrumental implementation, and characterization of a calibrated industrial hardness PTR system and report on its ability to measure case depth in hardened aerospace steels and gear teeth.

2. Three-Dimensional PTR Theoretical Model

To properly describe photothermally the hardness depth profile of industrial steels, we have developed a 3-D model to study the thermal-wave interferometric effects of finite beam sizes in inhomogeneous materials [16]. With this model, a case-hardened steel sample is treated as an axially inhomogeneous system that contains a thermophysically continuously inhomogeneous hardened layer and a homogeneous substrate (i.e., unhardened bulk). The physical parameters in the inhomogeneous layer, such as microhardness, thermal conductivity k, and thermal diffusivity α, are functions of depth as shown in Fig. 1. Figure 1(a) shows a typical microhardness profile of a hardened steel sample measured with a mechanical indentation method (HV0.5). It is well known that hardness decreases with depth. The effective case depth E is the distance below the surface where hardness drops to 513 HV (Vickers pyramid number), or 0.86 mm in this specific case. Figure 1(b) is a diagram of the inhomogeneous layer, which is divided into n virtual layers thin enough so that each layer can be considered thermophysically homogeneous, that is, the thermal conductivity k_i and thermal diffusivity α_i are constant within the layer of thickness L_i. An intensity-modulated Gaussian laser beam at frequency f, with radius a and power P, impinges normally on the sample along the z axis. The temperature increase in region i satisfies the thermal-wave equation

$$\nabla^2 T_i(r,z,\omega) - \sigma_i^2 T_i(r,z,\omega) = 0, \qquad (1)$$

where $\sigma_i = (1+j)\sqrt{\omega/2\alpha_i}$ is the complex thermal wavenumber and $\alpha_i = k_i/\rho_i c_i$ is the thermal diffusivity of layer i. Boundary conditions consist of temperature and heat flux continuity at all boundaries except for the front interface $z = 0$. At $z = 0$ the heat flux conservation condition is

$$k_0 \frac{\partial T_0(r,0,\omega)}{\partial z} - k_1 \frac{\partial T_1(r,0,\omega)}{\partial z} = Q_s(0), \qquad (2)$$

where

$$Q_s(0) = \frac{A_s(1-R_1)P}{\pi a^2} e^{-r^2/a^2}. \qquad (3)$$

R_1 and A_s represent the surface reflectance and absorptance of the sample, respectively, and a is the radius of the laser beam. Using the Hankel transformation of the thermal-wave fields [15], the inverse Hankel transform at the opaque sample surface can be obtained. It represents the surface thermal-wave field, which is the quantity directly measured by PTR:

$$T_i(r, z=0, \omega) = \int_0^\infty \tilde{T}(\lambda, z) = 0, \omega) J_0(\lambda r) \lambda \mathrm{d}\lambda, \qquad (4)$$

where J_0 is the Bessel function of the first kind of order zero, λ is the Hankel variable, and quantities

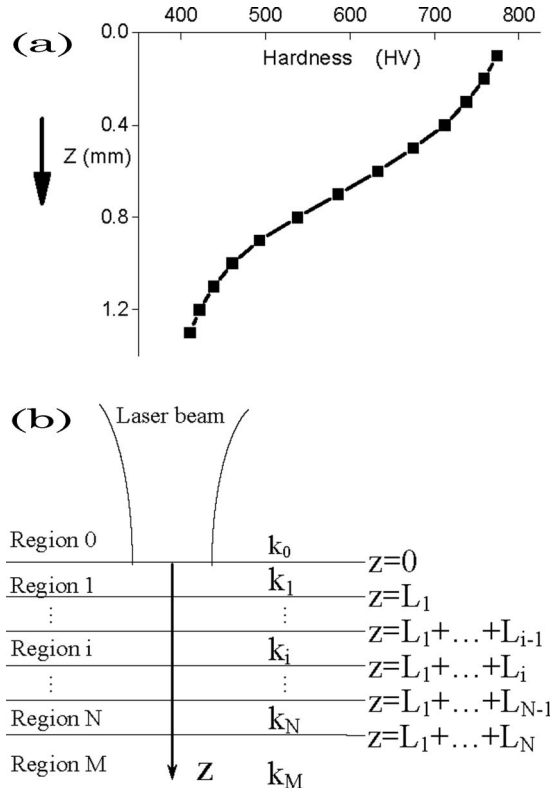

Fig. 1. (a) Typical microhardness profile of a hardened steel sample measured with the mechanical indentation method HV0.5. Hardness decreases with depth. The effective case depth E is the depth where the hardness drops to 513 HV, i.e., 0.86 mm in this case. (b) Schematic diagram of a continuously inhomogeneous system including an inhomogeneous layer and a substrate m. The inhomogeneous layer is divided into n layers for theoretical treatment.

with a tilde represent Hankel transforms. A convenient *ad hoc* thermal conductivity depth profile is assumed [17]:

$$k = k_0\left(\frac{1+\Delta e^{-qz}}{1+\Delta}\right), \tag{5}$$

where

$$\Delta = \frac{1-\sqrt{k_{L_0}/k_0}}{\sqrt{k_{L_0}/k_0 - e^{-qL_0}}}. \tag{6}$$

Here, k_0 and k_{L_0} represent the values of the thermal conductivity at two boundary surfaces, $z = 0$ and L_0, respectively. L_0 is the total thickness of the inhomogeneous layer and q is a curvature factor. Figure 2 shows that Eqs. (5) and (6) are capable of describing all possible monotonic curves with depth. It can be seen that Eq. (5) is adequate for expressing arbitrary monotonic profiles if parameters are properly chosen. The profile of the thermal conductivity is determined by the combination of k_0, k_{L_0}, q, and L_0.

The effect of beam size a was simulated assuming the parameters of the case-hardened layer to be as follows: $k_0 = 20\,\mathrm{W/mK}$, $k_{L_0} = 36.0489\,\mathrm{W/mK}$, $q = 2529\,\mathrm{mm^{-1}}$, and $L_0 = 2.45\,\mathrm{mm}$. In all simulations the unhardened substrate is assumed to be AISI 9310 steel, the thermophysical parameters of which are $k = 36.049\,\mathrm{W/mK}$, $\rho = 7750\,\mathrm{g/cm^3}$, and $c = 493.93\,\mathrm{J/kg\cdot °C}$ [18]. The depth profile of the thermal conductivity of the hardened layer is shown in Fig. 3. Figure 4 shows the amplitude and phase of a thermophysically inhomogeneous system, the frequency response of each quantity normalized by that generated with the same beam size from semi-infinite unhardened homogeneous AISI 9310 steel. It is seen from Fig. 4 that the amplitude and phase

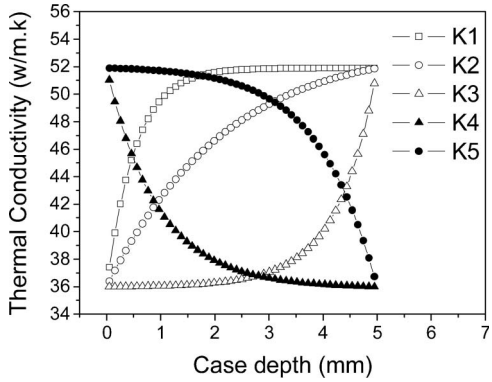

Fig. 2. Various thermal conductivity depth profiles obtained using the $k(z)$ ansatz, Eq. (5). The parameters used are as follows: curve K1, $k_0 = 36\,\mathrm{W/mK}$, $k_{L0} = 51.9\,\mathrm{W/mK}$, $q = 2\times10^3\,\mathrm{mm^{-1}}$, $L_0 = 5\,\mathrm{mm}$; curve K2, $k_0 = 35\,\mathrm{W/mK}$, $k_{L0} = 51.9\,\mathrm{W/mK}$, $q = 0.5\times10^3\,\mathrm{mm^{-1}}$, $L_0 = 5\,\mathrm{mm}$; curve K3, $k_0 = 36\,\mathrm{W/mK}$, $k_{L0} = 51.9\,\mathrm{W/mK}$, $q = -2\times10^3\,\mathrm{mm^{-1}}$, $L_0 = 5\,\mathrm{mm^{-1}}$; curve K4, $k_0 = 51.9\,\mathrm{W/mK}$, $k_{L0} = 36\,\mathrm{W/mK}$, $q = 1\times10^3\,\mathrm{mm^{-1}}$, $L_0 = 5\,\mathrm{mm}$; and curve K5, $k_0 = 51.9\,\mathrm{W/mK}$, $k_{L0} = \mathrm{W/mK}$, $q = -1\times10^3\,\mathrm{mm^{-1}}$, $L_0 = 5\,\mathrm{mm}$.

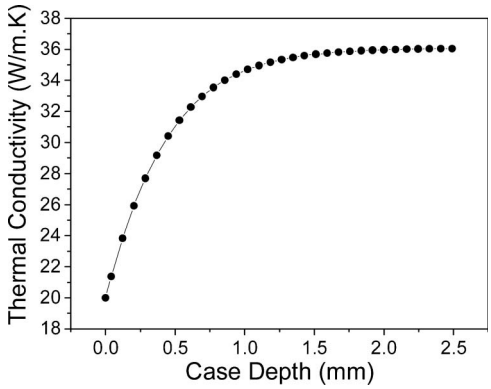

Fig. 3. Thermal conductivity depth profile of the hardened layer. Parameters used are $k_0 = 20\,\mathrm{W/mK}$, $k_{L0} = 36.0489\,\mathrm{W/mK}$, $q = 2529\,\mathrm{mm^{-1}}$, and $L_0 = 2.45\,\mathrm{mm}$.

are very sensitive to beam size. With increasing beam size from 0.01 mm (3-D limit) to 100 mm (1-D limit), the magnitude and frequency positions of the normalized phase minimum decrease and shift to lower frequencies. This can be understood when consideration is given to the relative sizes of the thermal diffusion length and beam size. In the approximate 1-D limit (large beam size) the diffusion length of the generated thermal wave matches the beam

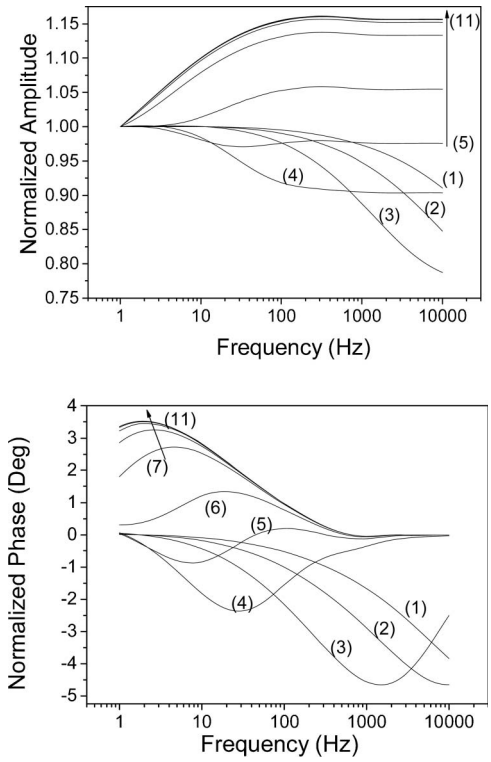

Fig. 4. Amplitude and phase of a steel with inhomogeneous thermal conductivity simulating a case-hardened AISI 9310 normalized by the corresponding homogeneous AISI 9310 semi-infinite steel sample using several beam sizes a (mm): (1) 0.01, (2) 0.02, (3) 0.05, (4) 0.5, (5) 1.0, (6) 2.0, (7) 5.0, (8)10, (9) 20, (10) 40, (11) 100. Other parameters of the hardened layer used are $k_0 = 20\,\mathrm{W/mK}$, $k_{L0} = 36.0489\,\mathrm{W/mK}$, $q = 2529\,\mathrm{mm^{-1}}$, and $L_0 = 2.45\,\mathrm{mm}$.

size at very low frequencies, contributing an interference phase maximum in the 1–10 Hz range. Since the case-hardened layer thermal conductivity is smaller than that of the bulk, the relative amplitude is larger than unity up to the size where the beam size leads to strictly 1-D behavior and the relative amplitude converges to unity (and the relative phase to zero) as shown in Fig. 4. With decreasing beam size the diffusion length-to-beam size equality is attained at higher frequencies as witnessed by the phase minimum shifts in Fig. 4(b). The additional (sideways) degrees of freedom in thermal-wave power conducted away from the laser source represent a loss to the local thermal-wave field, resulting in lower amplitudes compared to the semi-infinite unhardened steel. This is manifested by the <1 normalized amplitudes in Fig. 4(a). When the beam size is larger than 1 mm, the minimum shown in the case of small beam sizes disappears and a maximum emerges and shifts toward lower frequencies. This minimum-to-maximum inversion occurs because at this limit the standing thermal wave within the hardened region clearly reaches the effective interface with the better conducting substrate/bulk, which makes the back-propagating contribution to the interference pattern sensitive to the (negative) sign of the interface coupling (depletion) coefficient [19] to yield conductive loss. This is opposite to the 3-D interference condition involving the diffusion length versus beam size equality, discussed above. In that case, the confinement of the thermal-wave power within the illuminated area amounts to an interference pattern of conductive gain within a layer of very similar thermophysical properties surrounding the illuminated spot. This leads to an interferometric phase extremum opposite to that generated by material interfaces. The phase maximum eventually saturates when beam size becomes larger than 20 mm. From Fig. 4 it is clear that the largest phase maxima can be obtained with either a very small beam size (<0.05 mm; strongest interference stemming from the condition of thermal-diffusion-length and beam-size equality attained at high frequencies) or a very large beam size (>5 mm; strongest interface depletion transport effect attained at very low frequencies). The minima appearing at high frequencies (>1000 Hz) are subject to experimental distortion and noise resulting from surface roughness [20]. On the other hand, low-frequency PTR signals with large beam sizes suffer from low signal-to-noise ratio (SNR). Therefore, in practice, the selection of beam size is a trade-off between measurement sensitivity and SNR and is usually set at ~ 1 mm for optimum phase curvature, as was the case in these measurements.

It has been found that the thermal conductivity is anticorrelated with microhardness [11–14]. As discussed above, for practical hardness case depth measurements characteristic interferometric minima (or maxima) in the photothermal phase are obtained within the range of laser-beam modulation frequencies such that the effective hardness layer thickness L is commensurate with the thermal-wave diffusion length:

$$\mu_H = (\alpha_H/\pi f)^{1/2}, \tag{7}$$

where α_H is the thermal diffusivity of the hardened layer and f is the characteristic frequency. Equation (7) shows that thermal-wave interference extrema occurring at smaller f correspond to larger case depths. Since the characteristic frequency often indicates a phase minimum ("trough") rather than a peak, it is denoted as $f_{\min}$ in this paper. In fact, the interference pattern can also manifest itself as a peak in the sense of an antinode.

3. Instrumentation, Materials, and Signal Analysis

A. HD-PTR System

The principle of PTR is based on the detection of changes in thermal radiation emission from a material surface as a result of the absorption of an intensity-modulated laser beam. The parameters measured are amplitude and phase of the IR emission at different modulation frequencies. Then the measured phase from a case-hardened material is normalized by the phase from the nonhardened material of the same type (reference) by subtracting the reference phase. Since the normalized phase is usually noisier than either sample or reference phases, it is smoothed before $f_{\min}$ is extracted. Therefore, data acquisition and signal processing are two important procedures for a fast and reliable hardness measurement.

A PTR hardness inspection PTR instrument ("HD-PTR" system) was developed specifically for industrial on-line measurement purposes. The diagram of the HD-PTR system is shown in Fig. 5. The system consists of three parts: laser source and control system, optical box, and sample compartment. Part I provides the semiconductor laser source and current controls. The laser is an 808 nm diode laser of 4.5 W dc output (Model VDM00018, Jenoptik, Jena, Germany), a laser controller, a thermoelectric cooler (TEC) controller for the infrared detector, and a computer for data acquisition and laser modulation. The laser is thermoelectrically cooled, and its output is coupled to a 200 μm optical fiber of 0.22 NA. The laser has a coaxial 635 nm pilot visible beam of 1 mW for easy sample alignment. The computer is equipped with a data acquisition (DAQ) card with two sets of analog input/output ports (Model NI-PCI-4461, National Instruments, Austin, Texas). It controls laser current modulation in a swept frequency model for frequency scan measurements, or at a constant frequency for beam focusing and sample alignment. The software operating system operates in a Windows/LabVIEW environment. Part II is a small box ($19 \times 19 \times 10$ cm^3 dimension), containing a TEC-cooled 2–5 μm mercury-cadmium-zinc-telluride (MCZT) detector (Model PVI-2TE-5, VIGO System

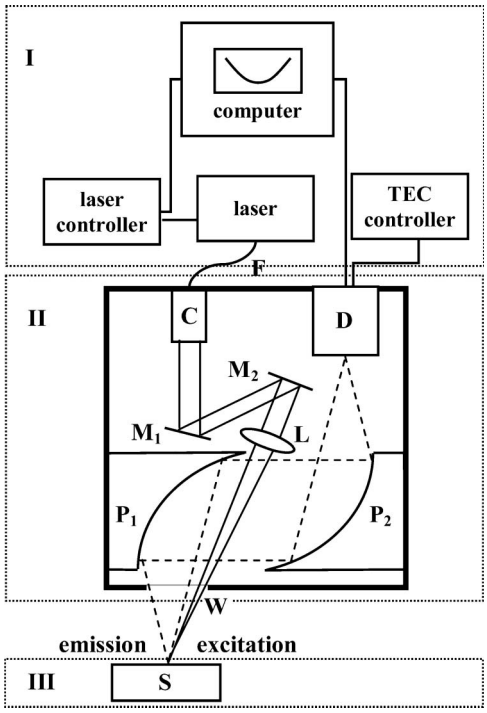

Fig. 5. Diagram of the HD-PTR system. The system consists of three parts. Part I: source and controlling system, including a diode laser, a laser controller, a detector TEC controller, and a computer for data acquisition and laser modulation. Part II: optical box, dimensions $19 \times 19 \times 10\,\mathrm{cm}^3$. F, optical fiber; C, collimator; D, TEC-cooled HgCdZnTe (MCZT) detector; M_1 and M_2, steering mirrors; L, lens; P_1 and P_2, gold-coated off-axis parabolic mirrors; W, CaF_2 window. Part III, S, sample compartment.

Ozarow Mazowiecki, Poland), a collimator, a pair of steering mirrors, a lens, a pair of gold-coated high-reflectance parabolic mirrors, and a CaF_2 window (99% transmission for both excitation and infrared emission spectral ranges). Part III is the sample compartment. The modulated laser beam is fiber-coupled into collimator C, Fig. 5. The collimated beam from C is steered into lens L by mirrors M_1 and M_2 and then focused onto sample S with a 0.7 mm diameter beam size and 16.4° angle relative to the normal of window W. The emitted IR signal is collected by parabolic mirror P_1 through the window W, and it is collimated and then focused onto the detector D by the parabolic mirror P_2. The signal from detector D is sent to the computer for processing.

Compared with the conventional bench-top PTR systems reported in the literature, the current HD-PTR system has the following advantages with respect to its use with hardened industrial steels:

- The measurement stability is increased by replacing the conventional liquid-nitrogen-cooled HgCdTe (MCT) detector with a TEC-cooled MCZT detector and isolating the delicate optics chamber from the heating laser and from the sample compartment.
- The measurement flexibility is increased by the compact optical box, which can be independently moved around to reach various sample measurement locations.
- The measurement speed is increased by replacing the conventional hardware lock-in amplifier with software swept-sine signal generation and detection modules.

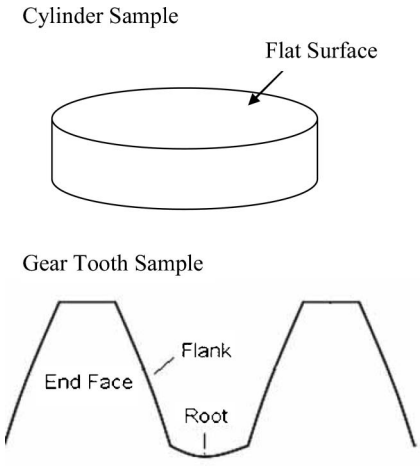

Fig. 6. Schematic cross section of cylindrical and gear-tooth samples, indicating the various measurement sites.

B. Industrial Steel Samples

Two types of industrial steel sample of different materials with cylindrical shape or gear-tooth shape were measured on sites of different geometries: large, flat surface (cross-sectioned slices of a cylinder normal to its center axis); a small flat surface (end face) of a gear tooth, a sloped surface of a gear tooth ("flank"), and a curved-surface gear tooth ("root") as shown in Fig. 6. Hardness E of the total of 13 samples and 18 sites varied from 0 to 1.78 mm; see Table 1. The samples with $E = 0$ mm were used as references to normalize the phase of the hardened steels. Each sample site was cleaned with methanol before measurement. The samples were put on an $x - y - z - \theta$ micrometer stage assembly so that the sample position and orientation could be changed as required.

C. PTR Signal Analysis

In our HD-PTR real-time hardness measurement system, Fig. 5, the swept sine method for fast frequency scans of industrial steel has the advantage of automatic adaptation of measurement settling time and data integration time with frequency to compensate for the low SNR at low frequencies and to speed up measurements at high frequencies, where the SNR is usually high. The settings used in these studies were: 5 cycles for signal settling and integration, and 1 s for settling and integration time. The HD-PTR system of Fig. 5 can perform a 30 point 1–500 Hz frequency scan within 1 min with a SNR of ~600 for PTR amplitude and 6000 for PTR phase as shown in Section 4. These PTR measurements were equally distributed in a logarithmic scale.

A finite laser beam size, 0.7 mm, was chosen for the HD-PTR system. From Fig. 4 we can see that such a

Table 1. Industrial Steel Sample Matrix for PTR Measurements

Name	Material	Shape	Measuring Site	Effective Case Depth (mm)
A1	AISI9310	Cylinder	Flat surface	1.78
A2	AISI9310	Cylinder	Flat surface	1.37
A3	AISI9310	Cylinder	Flat surface	0.61
A4	AISI9310	Cylinder	Flat surface	0
SA1	AISI9310	Cylinder	Flat surface	Unknown
C1	32CDV13	cylinder	Flat surface	0.41
C2	32CDV14	cylinder	Flat surface	0.31
C3	32CDV15	cylinder	Flat surface	0.21
C4	32CDV16	Cylinder	Flat surface	0
A_R	AISI9310	Gear tooth	End face	0
N2	18NiCr16	Gear tooth	Root	0.89
N3	18NiCr16	Gear tooth	root	0.97
N_R	18NiCr16	Gear tooth	root	0
N2	18NiCr16	Gear tooth	Flank	1.03
N3	18NiCr16	Gear tooth	Flank	1.16
N_R	18NiCr16	Gear tooth	Flank	0
N3	18NiCr16	Gear tooth	End face	1.25
N_R	18NiCr16	Gear tooth	End face	0

finite beam size results in a well-defined minimum in the 1–500 Hz range. The advantages of using this beam size are rooted in the utility of this frequency range. To begin with, the responses of the detector, laser, and DAQ card are optimal in this frequency range. Too high or too low a frequency range (corresponding to larger or smaller beam size, respectively) limits the instrumental sensitivity to hardness depth profiles. Next, fast and reliable measurements can only be achieved within this frequency range. To achieve the same SNR working at lower frequencies with a larger beam size takes a much longer time to scan the full frequency range. In addition, measurements in the 1–500 Hz frequency range are less sensitive to sample surface conditions (roughness and particle contamination) than at higher frequency ranges. In conclusion, the chosen frequency range minimizes preparation and scan-time requirements for real-time industrial sample inspection. Experimenting with various beam sizes proved that an ~0.7 mm beam size was optimal and yielded the best-case depth resolution.

To obtain the minimum frequency, the PTR signal (phase) was first normalized by subtracting the PTR phase of the hardened sample from that of the nonhardened sample (reference) of the same type of material and the same measuring site. The requirement for the same measuring site is to eliminate the geometry effect of gear-tooth samples, which often distorts the resulting minima and makes the extraction of minimum frequency difficult.

Phase was the PTR channel of choice throughout this work instead of amplitude for several reasons (also to be discussed in Section 4). Most importantly, phase is independent of the reflectivity of the sample surface, so it can be used as a "true" thermal-wave channel when industrial steels of unknown and/or uncontrollable surface conditions are involved. In order to compute $f_{\min}$, the normalized phase data with 30 points were first smoothed using the Savitzky–Golay filter [21]. The Savitzky–Golay filter smoothes a noisy signal by the piece-by-piece fitting of a polynomial function to the signal. The Savitzky–Golay smoothing filter is a type of filter first described in 1964 by Savitzky and Golay [21]. The Savitzky–Golay method essentially performs a local polynomial regression (of degree k) on a distribution (of at least $k+1$ equally spaced points) to determine the smoothed value for each point. The main advantage of this approach is that it tends to preserve features of the distribution such as relative maxima, minima, and width, which are usually "flattened" by other adjacent averaging techniques (such as moving averages). The normalized 30 experimental phase data points were interpolated into 120 points by means of the Savitzky–Golay filter process to produce a better curve fit and to increase the frequency resolution. Once the smoothed and interpolated phase was computed, the minimum frequency, $f_{\min}$, was extracted from the smoothed data.

4. Results and Discussion

A. System Thermal Transients and Measurement Optimization Controls

To make fast and reliable measurements, the system and measurement controls such as SNR, sample thermal transients, positioning effects, and sample surface treatment were investigated first. Fast frequency scan measurements usually suffer from low SNR at low frequencies owing to the $1/f$ noise characteristics of the detector. To compensate, the measurement speed must decrease. Employing a swept sine as the excitation waveform in our HD-PTR system offers a compromise between signal quality and speed. It allows setting signal settling and integration times both as sweep time and number of cycles. Thus one may use an optimal time-cycle combination to decrease the frequency scan at lower frequencies for higher SNR and increase it at higher frequencies where SNR is high. Figure 7 displays the PTR SNR from the end face measurement of an A-type nonhardened gear-tooth sample in the 1–500 Hz frequency range. No significant changes in the SNR of the PTR amplitude are observed [Fig. 7(a)]. For the phase, which is the main probe channel of the hardness case depth, the SNR is much higher at lower frequencies as indicated in Fig. 7(b).

A 200 s time scan at 10 Hz was performed on a cylindrical hardened sample, A3 ($E = 0.61$ mm), to study the sample thermal transient generated by laser heating. The laser was allowed to thermalize for 5 min (laser settling time) before the onset of the measurements. Both amplitude and phase in Fig. 8 show a fast transient during the initial period, followed by steady state (phase), while the amplitude still grows slowly. To see the detailed transient process, the time scan is divided into two time ranges and replotted in Figs. 9 and 10. Figure 9 shows the initial transient period, 0 to 8 s. The fast

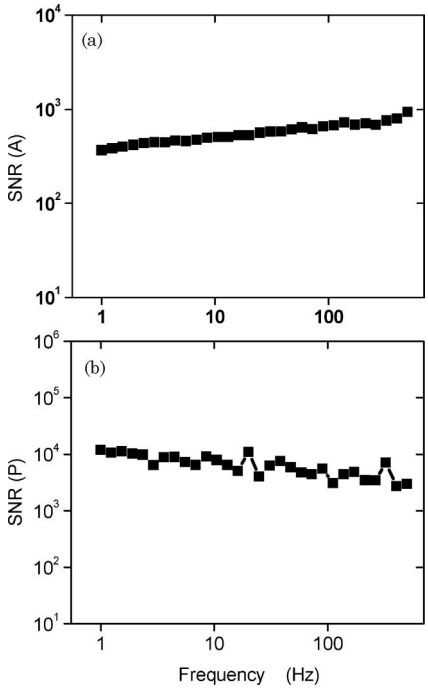

Fig. 7. PTR SNR versus frequency from the end face measurement of an A-type nonhardened gear-tooth sample (Table 1). The instrumental settling and integration time is 1 s, and the number of cycles for settling and integration is 5. 30 measured points cover a frequency span of 1–500 Hz. (a) SNR of PTR amplitude and (b) SNR of PTR phase.

transient lasts only for about 7 s. In Fig. 9(a), the amplitude rises from 0 to 1.75 mV during this period, while the phase shifts upward from about 150° to 330° in Fig. 9(b). For the long-term transient period (8–200 s) displayed in Fig. 10, the amplitude keeps growing at a relatively slow rate to 1.9 mV at the end of a 200 s period, an approximate 9% increase after the initial transient. In contrast, the phase remains stable at 333.8° with only 333.8° variation for the rest of the 200 s period after the initial transient. The initial transient time might be the instrument response time, including detector and DAQ card. This indicates that a waiting time of 7 s is needed before the onset of data acquisition. This defines waiting time in the PTR measurements. The PTR amplitude is more laser-heating sensitive to the steel temperature change than the phase. The attainment of phase steady state is most likely the result of the onset of independence from temperature of the steel thermophysical properties, even when temperature (and thus PTR amplitude) still grows. In this sense, amplitude is not a good parameter for fast measurements, whereas the stability of phase guarantees fast PTR measurement reliability.

To maximize measurement reproducibility and SNR, samples must always be positioned at the focal point of parabolic mirror P_1 in Fig. 2. In practice, it is hard to find this position. Sample misalignment effects on measurement reproducibility were studied using the cylindrical hardened sample, A3; see Table 1. After the amplitude was stabilized (by heating the sample with the laser for 20 min) the sample surface position was gradually scanned backward and forward away from the laser focal position ($z = 0$) over 21 steps using the translation stage. At each step, PTR amplitude and phase were measured at 10 Hz. The results are plotted in Fig. 11. Both amplitude and phase show a symmetric

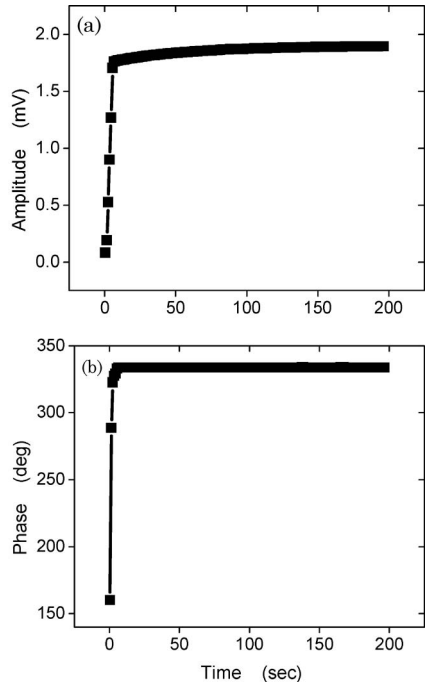

Fig. 8. Time scan (200 s) of a PTR signal at 10 Hz from a cylindrical hardened sample, A3. The measurements were taken after the laser had thermalized for 5 min. (a) PTR amplitude and (b) PTR phase.

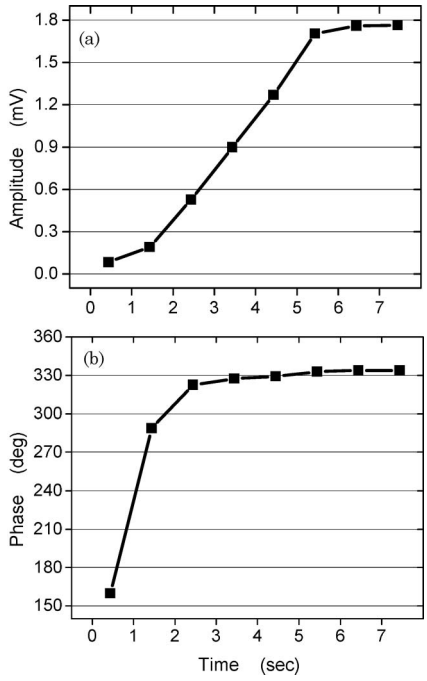

Fig. 9. Initial transient (0–8 s) of the PTR signal in Fig. 8: (a) amplitude and (b) phase.

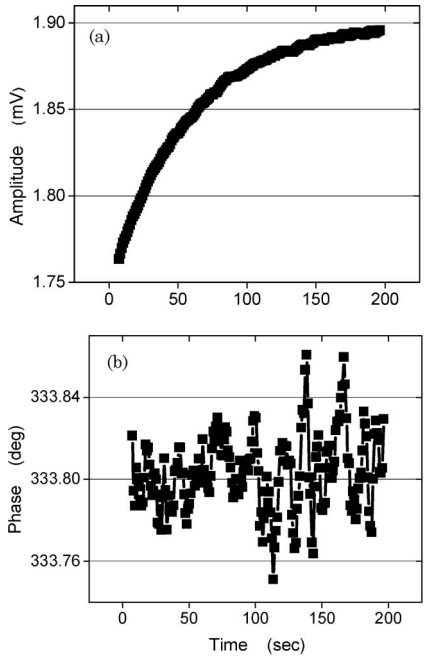

Fig. 10. Long-term transient (0–200 s) of the PTR signal in Fig. 8: (a) amplitude and (b) phase.

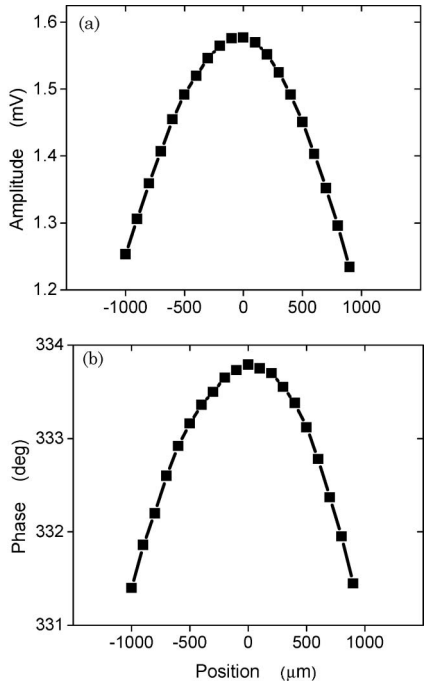

Fig. 11. Sample positioning effect on the PTR signal at 10 Hz from the cross section of the cylindrical hardened sample, A3. The sample was translated 1000 μm backward and forward, away from the laser focal position ($z = 0$) after PTR amplitude stabilization: (a) amplitude and (b) phase.

distribution around the focal position. The signal drops (amplitude 24%, phase 3.5°) when the sample surface is moved 1 mm away from the focal position. Figure 11 indicates that sample positioning away from the laser focus reduces measurement reproducibility and thus hardness measurement resolution. For example, a 400 μm sample displacement will cause 0.5° phase uncertainty in hardness case depth determination. However, this strong symmetric sample displacement, in fact, provides an easy sample positioning procedure for fast industrial inspection through a search for the maximum amplitude and/or largest phase signal. Even though amplitude and/or phase can be used for this procedure, phase is by far the better choice given the thermalization steady-state attainment within 7 s.

For PTR measurements, the sample surface is usually cleaned with a solvent such as methanol before measurement to remove contaminants (including oil and finger prints), which may cause changes in the PTR signal. However, besides being impractical for fast on-line measurements, this procedure may pose a potential danger to industrial materials covered with a thin film of oil. The removal of the oil layer will accelerate metal surface oxidization, resulting in hardness decrease as discussed in Subsection 4.D. To study the effect of thin oil films on the PTR signal, a nonhardened gear-tooth sample (A_R, end face) was measured before and after the removal of the oil layer with methanol as shown in Fig. 12. The PTR amplitude is affected greatly, with about a 45.5% drop on average after the removal of the oil layer [Fig. 12(a)]. For example, at 1 Hz, the amplitude falls from 24.4 to 13.58 mV. However, the phase is not affected much at all by removal of the oil layer, indicated by the two almost overlapping curves [Fig. 12(b)]. The detailed absolute phase difference is plotted in Fig. 12(c). It can be seen that the oil effect is nonmonotonically frequency dependent. At low frequencies (~1 Hz) and high frequencies (~500 Hz) the phase difference due to the presence of an oil layer is ~0.2° (~0.05% change), whereas the phase difference is below 0.1° (<0.02% change) in the range 10–180 Hz. Since the PTR phase is the channel of choice for hardness case depth measurements and the minimum frequency $f_{\min}$ usually appears within the 10–180 Hz range for the hardness case depth ranges of industrial interest, the surface oil film effect is negligible, and a surface cleaning procedure is not required for on-line steel hardness inspection.

B. Multichannel Hardness Measurements

To evaluate the unknown hardness case depth of steel samples, calibration curves were obtained from the phase measurement of individual hardened samples with different known and independently measured effective case depths as shown in Fig. 13. Figure 13(a) shows a typical phase minimum ("trough") from the cylindrical hardened sample Al ($E = 1.78$ mm). The symbols represent data points, and the continuous line is the best-fitted curve. A photothermal trough/peak extremum can be described by three parameters: minimum frequency $f_{\min}$, trough/peak width W, and area $S = \sum \Delta f_i P_i$. Figure 13(b) displays troughs from two root measurements of the N-type gear-tooth

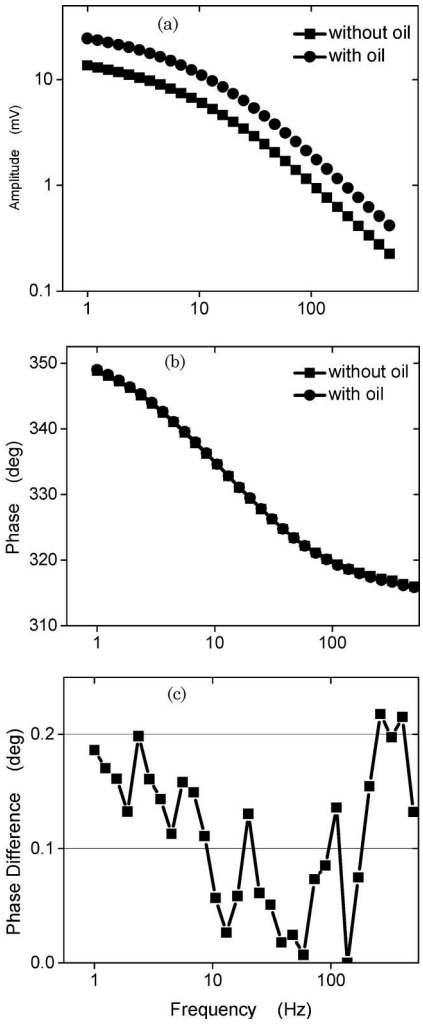

Fig. 12. Thin oil-film effect on PTR signal. The end face of a non-hardened gear-tooth sample, A_R, was probed before and after the protective oil layer was removed with methanol: (a) amplitude, (b) phase, (c) absolute phase difference between the measurements with and without the oil film.

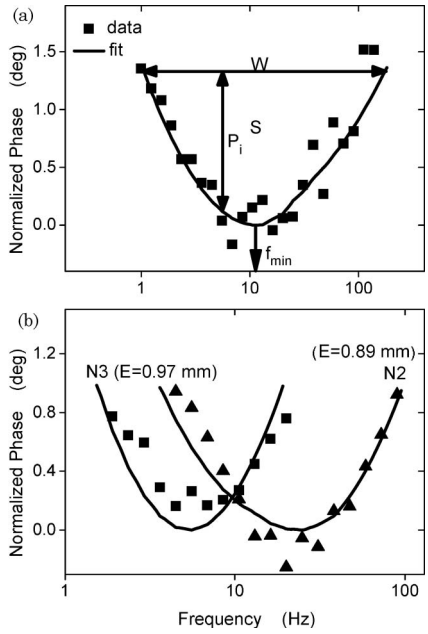

Fig. 13. Three parameters extracted from normalized PTR phase frequency scans: minimum frequency f_{min}, trough/peak width W, and area S, and their correlation with sample hardness E: smaller f_{min}, W, and S indicate deeper effective case depth. (a) Typical trough shape from the cylindrical hardened sample A1; (b) troughs from two root measurements of N-type gear-tooth samples, N2 ($E = 0.89$ mm) and N3 ($E = 0.97$ mm).

samples, N2 ($E = 0.89$ mm) and N3 ($E = 0.97$ mm). It was found that not only f_{min} but also W and S are correlated with sample hardness: smaller f_{min}, W, and S indicate a larger effective case depth. In fact, W and S were found to be very stable parameters with respect to repeatability and reproducibility measurements at the end face of the N3 sample as shown in Table 2. The variations of W and S over 10 continuous (no sample removal) and 10 individual (with sample removal and reloading) measurements are less than that of f_{min}. However, the three metrics are not interchangeable. They are complementary for hardness measurements in different ranges of case depth. Figure 14 shows the calibration curves for the three parameters for cylindrical A-type samples with effective case depths ranging from 0.61 to 1.78 mm (indicated by their hardness profiles measured by indentation method). It can be seen that the W and S curves exhibit much higher gradient —and therefore higher sensitivity—in the shallow case depth range (0.61–1.37 mm) than f_{min}. In the medium case depth range (1.03–1.16 mm) of the N samples, the three parameters have comparable sensitivity as shown in Fig. 15. It was further verified that W and S are most reliable for shallow case depths characteristic of the cylindrical C-type samples. The effective case depths of this set of samples were between 0.21 and 0.41 mm. The phase curvature was very small, so that f_{min} could not resolve them. However, W and S measurements resolved these case depths very well as shown in Fig. 16. It is noticed that the trends are opposite to the previous measurements: smaller W and S indicate shallower

Table 2. Repeatability and Reproducibility Measurements on the End Face of the N3 Sample

	Repeatability (10 Continuous Measurements)			Reproducibility (10 Individual Measurements)		
Metrics	Average	STDEV	Variation (%)	Average	STDEV	Variation (%)
f_{min}	10.19	0.23	2.25	10.20	0.25	2.41
W	43.43	1.01	2.32	43.04	0.72	1.68
S	74.92	0.49	0.65	73.74	0.87	1.18

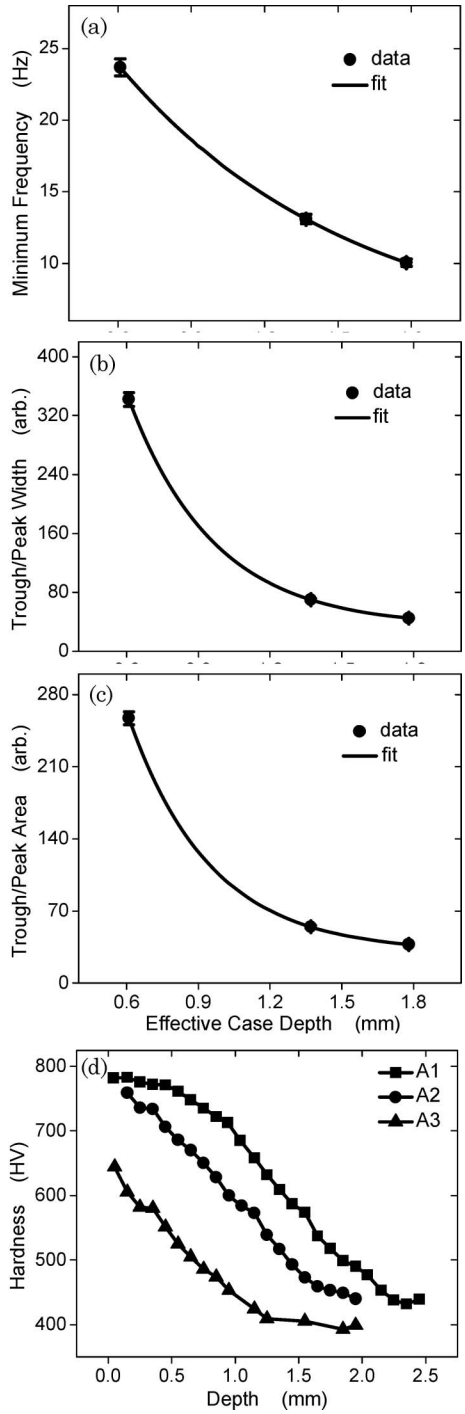

Fig. 14. Correlation between PTR phase trough parameters and hardness of cylindrical sample set A: A1 ($E = 1.78$ mm), A2 ($E = 1.37$ mm), and A3 ($E = 0.61$). (a) E versus f_{min}, (b) E versus W, (c) E versus S, (d) hardness profiles measured by the indentation method.

case depth. This is so because the phase curvature has changed to a peak from a trough, as predicted by the theory. This phase inversion can be encountered in thermal-wave interferometry with certain combinations of laser spot size and thermophysical properties of materials [16], including thermal conductivity, diffusivity, and their depth profiles.

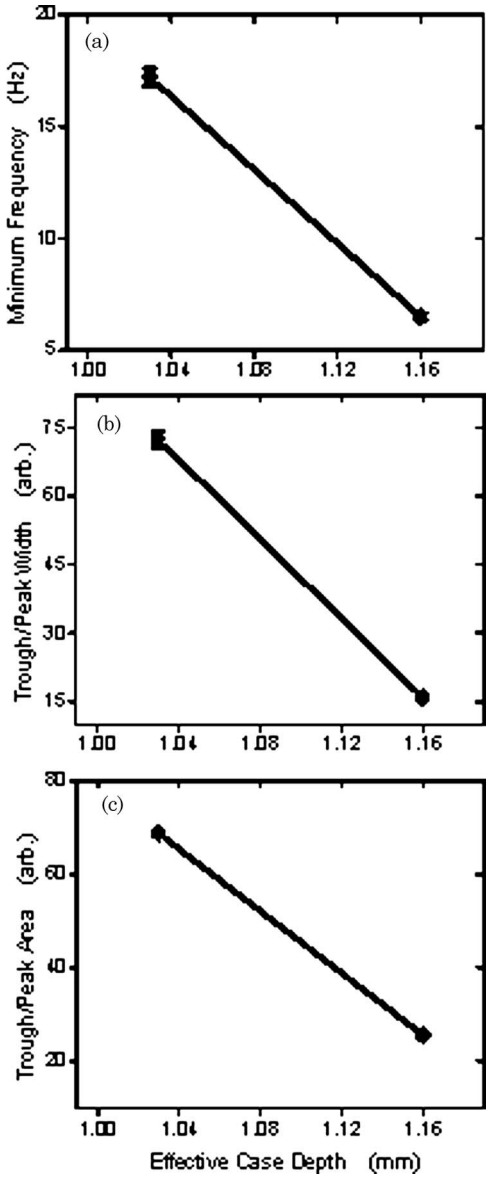

Fig. 15. Correlation between PTR phase trough parameters and flank hardness of gear-tooth sample set N: N3 ($E = 1.16$ mm), N2 ($E = 1.03$). (a) E versus f_{min}, (b) E versus W, (c) E versus S.

Using the calibration curves in Fig. 14, the case depth of an unknown cylindrical sample SA1 was evaluated. The results are shown in Table 3. It is seen that the estimated effective case depth of sample SA1 from the f_{min} measurement is 1.46 mm, very close to the 1.49 mm value obtained by indentation. The W and S measurements yielded 1.73 and 1.69 mm, respectively. These results show that f_{min} is a much more accurate measure of case depths than W and/or S for large case depths.

C. Angular Incidence Dependence of Hardness Measurement Resolution

It was found from our experiments that the orientation (angle) of the sample surface with respect to the laser beam sensitively affects hardness measurement resolution. Figure 17(a) shows the angular

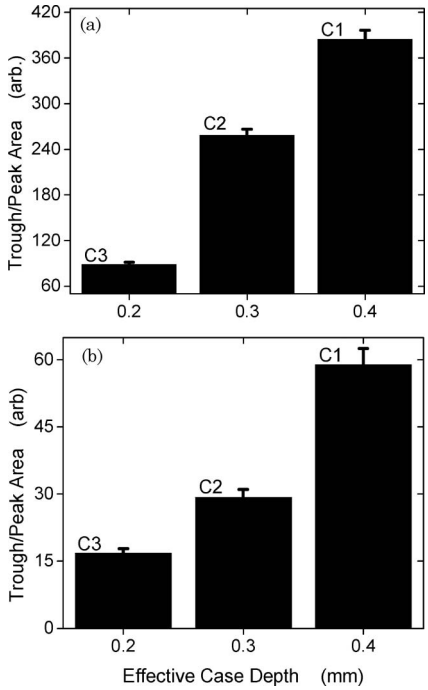

Fig. 16. Correlation between PTR phase peak parameters and hardness of cylindrical sample set C: C1 ($E = 0.41$ mm), C2 ($E = 0.31$ mm), and C3 ($E = 0.21$). (a) E versus S, (c) E versus W.

geometry. Figures 17(b)–17(d) show the results of the angular dependence measurements. Calibration curves of the A-type cylindrical samples A1 ($E = 1.78$ mm), A2 ($E = 1.37$ mm), and A3 ($E = 0.61$ mm) were obtained from measurements at various sample angles from 0° (sample face parallel with the CaF_2 window, Fig. 2) to 15° (sample face almost perpendicular to the laser beam, Fig. 17(a)). The hardness measurement resolution of f_{min}, W and S varies greatly with sample angle. In general, a 5° sample orientation is the optimal measurement angle. The observed angular dependence could be interpreted as due to the projectional beam-size effects on the surface plane of the sample. When the sample surface is nearly normal with respect to the laser-beam axis, the beam size on the sample decreases, which in turn affects the measurement resolution of thermal properties [19].

D. Surface Oxidation Effect on Steel Hardness Case Depth Measurements

When hardened steel samples are exposed to the ambient without a protective oil layer, they easily be-

Table 3. Unknown Sample SA1 Evaluation

Estimated Effective Case Depth by Measurement in mm			Effective Case Depth Measured by Indentation(513 HV) (mm)
f_{min}	W	S	
1.46	1.73	1.68	1.49

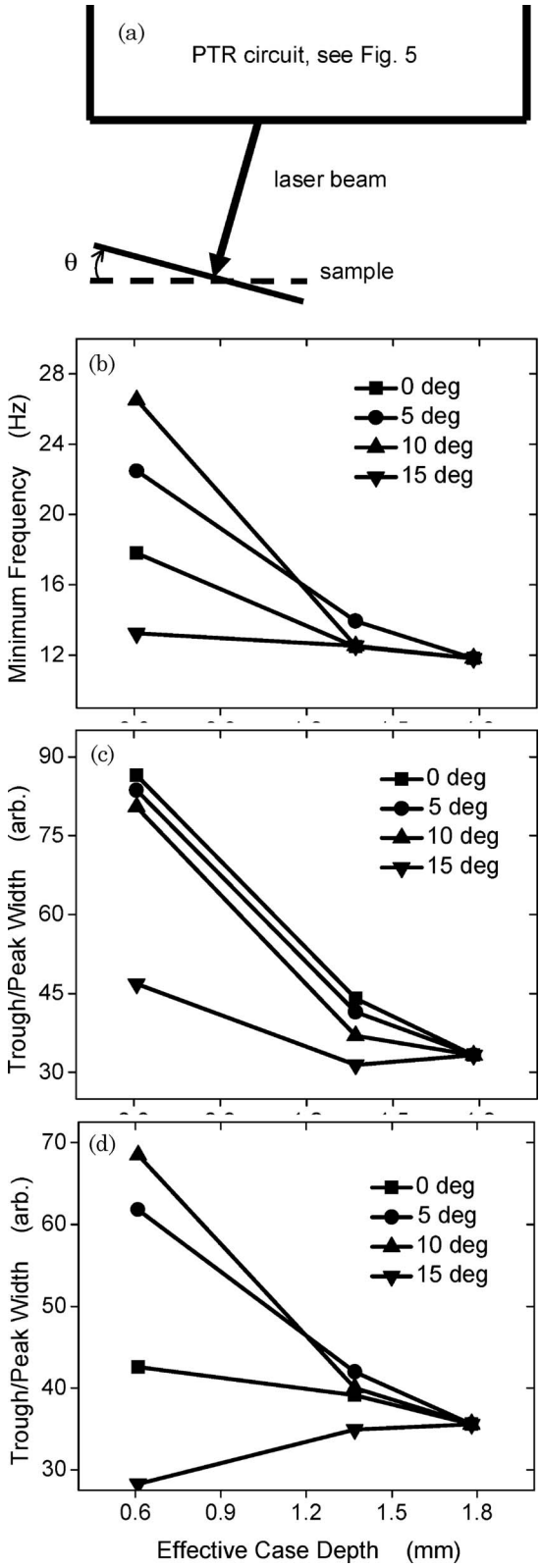

Fig. 17. Hardness measurement resolution dependence on angle between sample-surface normal and laser-beam axis. A-type cylindrical samples A1 ($E = 1.78$ mm), A2 ($E = 1.37$ mm), and A3 ($E = 0.61$) were measured at different angles from 0° to 15° (almost perpendicular to the laser beam). $\theta = 5°$ was found to be the optimal measurement angle. (a) Laser-beam and sample surface geometry and angle definition, (b) E vesus f_{min}, (c) E versus W, (d) E versus S at various angles.

come oxidized, acquiring a brownish layer. From measurements at end faces of two N3 gear-tooth samples it was found that oxidization reduced the effective measured hardness case depth. These two samples, denoted as N3 and N3S, were cut from the same gear and originally hardened under the same conditions. The hardness case depth at the end face was 1.25 mm as determined by the mechanical indentation method. The two samples were stored under different conditions. N3S became severely oxidized and exhibited a dark-brown surface. To simplify the data interpretation, the N3S oxide layer was removed before measurement by sandblasting, a well-known process for cleaning a hard surface by forcing solid particles across that surface at high speeds. The measurement results, presented in Table 4, show that all three measured parameters, $f_{\min}$, W, and S, of N3S are higher than those of the unoxidized N3. The increase of $f_{\min}$, W, and S implies a decrease in hardness case depth. This phenomenon can be interpreted in view of the fact that oxidation damages the hardest top layer, resulting in a shallower effective case depth. The foregoing measurement results underscore the importance of oxidation prevention of hardened samples to be measured by photothermal techniques.

5. Conclusions

Photothermal radiometry is a nondestructive evaluation method that has excellent potential for monitoring the effective case depth of case-hardened steel samples. PTR phase measurement can yield reliable and accurate calibration curves for case depth evaluation in a very wide range of hardened case depths. What is to our knowledge the first industrial-level hardness HD-PTR instrumentation system has been developed and built, guided by laser photothermal interferometric principles. The system stability, the signal quality for fast measurements, repeatability, and reproducibility have been tested. A series of industrial steel samples, flat or curvilinear, with various effective case depths (0.21–1.78 mm) were measured both photothermally and destructively using mechanical indentation to obtain calibration curves. The factors affecting hardness resolution were investigated. Our results demonstrated that PTR phase has high stability with less than 0.1° variation during a 3 min measurement period, which covers the hardness measurement time at an industrial site (1 min). The system exhibits less than 2.7% variation over 10 repeated, reproducible measurements of three phase parameters, namely, interference minimum frequency $f_{\min}$, peak/trough width W, and area S. It has been found from the calibration curves that $f_{\min}$, W, and S are complementary metrics to evaluate hardness case depth: $f_{\min}$ performs optimally with large case depth profiles, whereas W and S are more suitable for shallow case depth measurements. With these three metrics, the HD-PTR system functionally spans very wide case depth ranges from ultrashallow ($E = 0.2$ mm) to very deep ($E = 1.78$ mm). It was also found that sample position and surface inclination with respect to the incident laser beam affects hardness measurement resolution. Sample positioning at the focal point of the laser beam can be easily achieved by tuning sample translation to the maximum phase signal. However, signal amplitudes and phases are strongly beam-size dependent. The optimal orientation angle of the sample surface normal for this system is between 6° and 11° with respect to the laser-beam axis. Our measurements demonstrated that the hardness case depth measured through the PTR phase-frequency response is not affected by the presence of a surface oil film but decreases with sample surface oxidation. To prevent oxidation, the protective oil film on the sample surface should not be removed.

Table 4. Oxidization Effects on the Sample Hardness

Sample	Surface Condition	Metrics		
		$f_{\min}$ (Hz)	W (Hz)	S (deg-Hz)
N3	Nonoxidized	10.05	123.89	358.35
N3S	Oxidized and sandblasted	13.09	450.54	1069.97

The authors thank Avio S.p.A. Italy for providing samples and Materials and Manufacturing Ontario (Ontario Centers of Excellence) and Avio for support of this instrumentation research.

References

1. A. Rosencwaig and A. Gersho, "Theory of the photoacoustic effect with solids," J. Appl. Phys. **47**, 64–69 (1976).
2. P. Nordal and S. O. Kanstad, "Photothermal radiometry," Phys. Scr. **20**, 659–662 (1979).
3. J. Shen and A. Mandelis, "Thermal-wave resonator cavity," Rev. Sci. Instrum. **66**, 4999–5005 (1995).
4. D. Fournier, A. C. Boccara, and J. Badoz, "Thermo-optical spectroscopy: detection by the "mirage effect," Appl. Phys. Lett. **36**, 130–132 (1980).
5. A. Salazar, A. Sanchez-Lavega, and J. M. Terron, "Effective thermal diffusivity of layered materials measured by modulated photothermal techniques," J. Appl. Phys. **84**, 3031–3041 (1998).
6. T. D. Bennett and F. Yu, "A nondestructive technique for determining thermal properties of thermal barrier coatings," J. Appl. Phys. **97**, 013520 (2005).
7. P. Li and G. Zhou, "Photothermal radiometry probing of scars in the internal surface of a thin metal tube," Appl. Opt. **31**, 3781–3783 (1992).
8. M. Depriester, P. Hus, S. Delenclos, and A. Sahraoui, "New methodology for thermal parameter measurements in solids using photothermal radiometry," Rev. Sci. Instrum. **76**, 074902 (2005).
9. M. Reichling and H. Gronbeck, "Harmonic heat flow in isotropic layered systems and its use for thin film thermal conductivity measurements," J. Appl. Phys. **75**, 1914–1922 (1994).
10. J. Jaarinøn and M. Luukkala, "Numerical analysis of thermal waves in stratified media for non-destructive testing purposes," J. Phys. (Paris) **44**, C6–503 (1983).
11. T. T. N. Lan, H. G. Walther, G. Goch, and B. Schmitz, "Experimental results of photothermal microstructural depth profiling," J. Appl. Phys. **78**, 4108–4111 (1995).

12. H. G. Walther, D. Fournier, J. C. Krapez, M. Luukkala, B. Schmitz, C. Sibilia, H. Stamm, and J. Thoen, "Photothermal steel hardness measurements–results and perspectives," Anal. Sci. **17**, s165–s168 (2001).
13. D. Fournier, J. P. Roger, A. Bellouati, C. Boué, H. Stamm, and F. Lakestani, "Correlation between hardness and thermal diffusivity," Anal. Sci. **17**, s158–s160 (2001).
14. M. Munidasa, F. Funak, and A. Mandelis, "Application of a generalized methodology for quantitative thermal diffusivity depth profile reconstruction in manufactured inhomogeneous steel-based materials," J. Appl. Phys. **83**, 3495–3498 (1998).
15. A. Mandelis, *Diffusion-Wave Fields: Mathematical Methods and Green Functions* (Springer, 2001), Chap. 3.
16. H. Qu, C. Wang, X. Guo, and A. Mandelis, "Reconstruction of depth profiles of thermal conductivity of case-hardened steels using a three-dimensional photothermal technique," J. Appl. Phys., to be published.
17. A. Mandelis, F. Funak, and M. Munidasa, "Generalized methodology for thermal diffusivity depth profile reconstruction in semi-infinite and finitely thick inhomogeneous solids," J. Appl. Phys. **80**, 5570–5578 (1996).
18. Standard SAE 9310, "Data on world wide metals and alloys," (SAE International, 1990), SA-444.
19. C. Wang, A. Mandelis, H. Qu, and Z. Chen, "Influence of laser beam size on measurement sensitivity of thermophysical property gradients in layered structures using thermal-wave techniques," J. Appl. Phys. **103**, 043510 (2008).
20. L. Nicolaides and A. Mandelis, "Methods for surface roughness elimination from thermal-wave frequency scans in thermally inhomogeneous solids," J. Appl. Phys. **90**, 1255–1265 (2001).
21. A. Savitzky and M. J. E. Golay, "Smoothing and differentiation of data by simplified least squares procedures," Anal. Chem. **36**, 1627–1639 (1964).